Progress In Electromagnetics Research B, Vol. 27, 253–272, 2011

COMPLEX IMAGE METHOD ANALYSIS OF A PLANE WAVE-EXCITED SUBWAVELENGTH CIRCULAR APERTURE IN A PLANAR SCREEN

K. A. Michalski

Department of Electrical and Computer Engineering
Texas A&M University, College Station, TX 77843-3128, USA

Abstract—A complex image method is presented for the analysis of a subwavelength circular aperture in a perfectly conducting screen of infinitesimal thickness illuminated by a plane wave. The method is based on the Bethe-Bouwkamp quasi static model of the aperture field and uses the spectral domain formulation as the point of departure. Closed-form expressions are obtained for the electromagnetic fields valid for all observation points. Sample numerical results demonstrate the accuracy and efficiency of the method for both normal and oblique illuminations, including an evanescent wave. In the latter case, the results show a circulating power flux and enhanced field confinement near the aperture.

1. INTRODUCTION

The problem of light transmission through a subwavelength aperture in a metallic screen continues to be of interest in the context of scanning near-field optical microscopy (SNOM) [1–3]. Important in these applications is not only the light transmission efficiency, but also the electromagnetic field distribution in the vicinity of the aperture, including the polarization effects. We limit attention here to a perfectly conducting screen of infinitesimal thickness with a circular aperture of radius $a \ll \lambda$, where λ is the wavelength. The first solution of this problem was put forward by Bethe [4], who derived a quasi-static expression for the aperture equivalent magnetic current, which was later corrected by Bouwkamp [5–7]. In spite of the assumption of an infinitely thin perfect conductor, the Bethe-Bouwkamp (BB) model has been extensively used in the aperture source characterization for SNOM applications [2, 8].

Received 16 October 2010, Accepted 26 November 2010, Scheduled 13 December 2010
Corresponding author: Krzysztof A. Michalski (krys@ece.tamu.edu).

The first numerical studies of the transmitted field distribution based on the BB aperture model were by Leviatan [9], Dürig et al. [10], and Nakano and Kawata [11], using the space domain method, and by Van Labeke et al. [12–14] and Grober et al. [15], using the spectral domain approach. The latter method has the advantage that the fields may be expressed as one-dimensional integrals [2, 14, 15], and that planar and layered dielectric samples may be easily incorporated in the formulation [3, 13, 14, 16]. Of all the studies mentioned above only Nakano and Kawata [11] considered the non-normal incidence case. However, Nakano and Kawata [11] (as well as Dürig et al. [10]) used Bethe's original magnetic current in their analysis, which differs from the correct Bouwkamp's expression by a solenoidal vector. Ducourtieux et al. [2] noted the desirability of extending the spectral domain method of Grober et al. [15] for non-axial illumination, but stated that "at off-normal angles of incidence $(\cdots)$ the theory appears to become numerically intractable at the moment."

The Hankel transform integrals that arise in the spectral domain approach must be evaluated numerically, which can be computationally expensive, since the integrations must be redone for every distinct observation point of interest. In the present paper, we describe an efficient complex image method, which makes it possible to evaluate the Hankel transforms analytically, and thus leads to closed-form expressions for the electromagnetic fields excited by the aperture source, valid for all observation points. The basic premise of this method is that the so-called aperture source functions, which characterize the spectrum of the BB aperture field distribution, can accurately be represented by a small number of complex exponential terms. We present sample numerical results that demonstrate the accuracy and efficiency of this method for both normal and oblique illuminations, including an evanescent wave. In the latter case, our results show a circulating power flux and enhanced field confinement near the aperture.

2. FORMULATION

The geometry of the problem and the coordinate system used are illustrated in Fig. 1. We assume that the screen resides in an isotropic homogeneous medium characterized by the wavenumber $k = \omega\sqrt{\epsilon\mu} = 2\pi/\lambda$ and intrinsic impedance $\eta = \sqrt{\mu/\epsilon}$, where ϵ and μ are the permittivity and permeability of the medium, respectively. The plane of incidence is chosen as the xz-plane, θ_i is the angle between the z axis and the direction of incidence, and ψ_i is the angle between $\mathbf{E}^i$ and the xz-plane. The polarization is parallel for $\psi_i = 0^\circ$ (TM wave) and

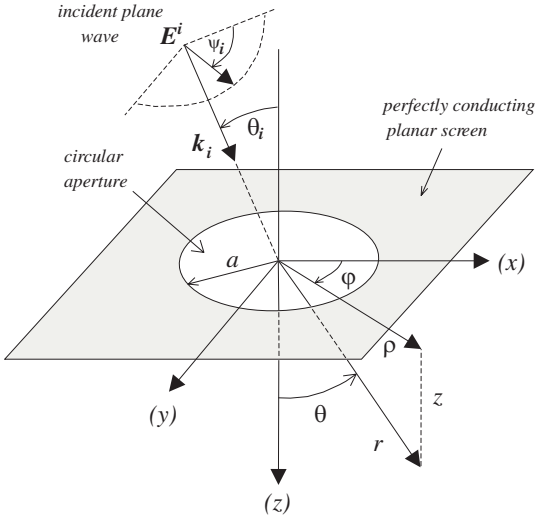

Figure 1. Diagram of a plane wave obliquely incident on the circular aperture in a planar screen, indicating the coordinate system used in the analysis.

perpendicular for $\psi_i = 90°$ (TE wave). Without loss of generality, the amplitude of the incident wave $\mathbf{E}^i$ is set to unity. In the Cartesian component notation, using the $e^{j\omega t}$ time convention and SI units, the electric and magnetic incident fields are given as

$$\mathbf{E}^i = (\kappa_{zi}\cos\psi_i, \sin\psi_i, -\kappa_{xi}\cos\psi_i)\, e^{-jk(\kappa_{xi}x+\kappa_{zi}z)}, \tag{1}$$

$$\eta\mathbf{H}^i = (-\kappa_{zi}\sin\psi_i, \cos\psi_i, \kappa_{xi}\sin\psi_i)\, e^{-jk(\kappa_{xi}x+\kappa_{zi}z)}, \tag{2}$$

where

$$\kappa_{xi} \equiv \frac{k_{xi}}{k} = \sin\theta_i, \quad \kappa_{zi} \equiv \frac{k_{zi}}{k} = \cos\theta_i, \tag{3}$$

are the normalized x and z components of the propagation vector $\boldsymbol{k}_i$. For generality, we also allow for an inhomogeneous plane wave, evanescent along the z axis [17], where κ_{xi} may be any real number with the corresponding κ_{zi} given as

$$\kappa_{zi} = \sqrt{1-\kappa_{xi}^2}, \quad \Im\mathrm{m}\,\kappa_{zi} \le 0\,. \tag{4}$$

Hence, κ_{zi} is positive for a homogeneous wave ($\kappa_{xi}^2 \le 1$) and negative imaginary for an evanescent wave ($\kappa_{xi}^2 > 1$).

In view of the equivalence principle [18, p. 110], the knowledge of the tangential electric field in the aperture plane ($z = 0$) is sufficient

to determine the electromagnetic field everywhere in the $z > 0$ half-space. According to the BB model, the tangential field components in the aperture ($\rho < a$) may be approximated as [6, 7]

$$\begin{aligned} E_x^a \;=\; & -\frac{2}{\pi}\,\kappa_{xi}\cos\psi_i\cos\varphi\,\frac{\rho}{\sqrt{a^2-\rho^2}} \\ & +\frac{2jk}{3\pi}\left\{\cos\psi_i\left(\frac{4a^2-3\rho^2}{\sqrt{a^2-\rho^2}}+\kappa_{xi}^2\,\frac{3\rho^2-2a^2}{\sqrt{a^2-\rho^2}}\right)\right. \\ & \left.+\left[(1+\kappa_{xi}^2)\cos\psi_i\cos 2\varphi+\kappa_{zi}\sin\psi_i\sin 2\varphi\right]\frac{\rho^2}{\sqrt{a^2-\rho^2}}\right\}, \end{aligned} \tag{5}$$

$$\begin{aligned} E_y^a \;=\; & -\frac{2}{\pi}\,\kappa_{xi}\cos\psi_i\sin\varphi\,\frac{\rho}{\sqrt{a^2-\rho^2}}+\frac{2jk}{3\pi}\left\{\kappa_{zi}\sin\psi_i\,\frac{4a^2-3\rho^2}{\sqrt{a^2-\rho^2}}\right. \\ & \left.+\left[(1+\kappa_{xi}^2)\cos\psi_i\sin 2\varphi-\kappa_{zi}\sin\psi_i\cos 2\varphi\right]\frac{\rho^2}{\sqrt{a^2-\rho^2}}\right\}, \end{aligned} \tag{6}$$

where the superscript a indicates that these expressions pertain to the aperture plane. Outside the aperture ($\rho > a$), $E_x^a = E_y^a = 0$.

In our spectral domain formulation we utilize the Fourier transform pair

$$\tilde{f}(k_x,k_y) \;=\; \int_{-\infty}^{\infty}\int_{-\infty}^{\infty} f(x,y)\,e^{j(k_x x+k_y y)}\,\mathrm{d}x\mathrm{d}y, \tag{7}$$

$$f(x,y) \;=\; \frac{1}{(2\pi)^2}\int_{-\infty}^{\infty}\int_{-\infty}^{\infty}\tilde{f}(k_x,k_y)\,e^{-j(k_x x+k_y y)}\,\mathrm{d}k_x\mathrm{d}k_y\,. \tag{8}$$

The Fourier transformation (7) of the aperture plane fields (5)–(6) yields

$$\begin{aligned} \tilde{E}_x^a \;=\; & -\frac{4ja^3}{3}\,\kappa_{xi}\cos\psi_i\,k_x F_1+\frac{4jka^3}{3}\left\{\cos\psi_i\left[(F_1+F_0)-\kappa_{xi}^2\,F_2\right]\right. \\ & \left.-\left[(1+\kappa_{xi}^2)\cos\psi_i\,(k_x^2-k_y^2)+2\kappa_{zi}\sin\psi_i\,k_x k_y\right]\frac{F_2}{k_\rho^2}\right\}, \end{aligned} \tag{9}$$

$$\begin{aligned} \tilde{E}_y^a \;=\; & -\frac{4ja^3}{3}\,\kappa_{xi}\cos\psi_i\,k_y F_1+\frac{4jka^3}{3}\left\{\kappa_{zi}\sin\psi_i\,(F_1+F_0)\right. \\ & \left.-\left[2(1+\kappa_{xi}^2)\cos\psi_i\,k_x k_y-\kappa_{zi}\sin\psi_i\,(k_x^2-k_y^2)\right]\frac{F_2}{k_\rho^2}\right\}, \end{aligned} \tag{10}$$

where we have introduced the notation

$$F_0 \;=\; j_0(k_\rho a), \tag{11}$$

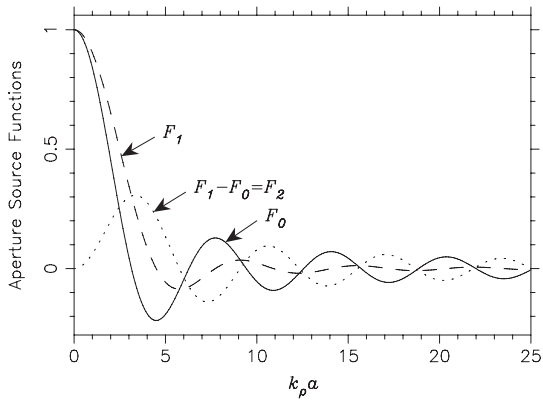

Figure 2. Plot of the aperture source functions.

$$F_1 = 3\,\frac{j_1(k_\rho a)}{k_\rho a}, \tag{12}$$

and

$$F_2 = F_1 - F_0 = j_2(k_\rho a), \tag{13}$$

where $k_\rho = \sqrt{k_x^2 + k_y^2}$ and j_n is the spherical Bessel function of order n. The functions F_i, $i = 0, 1, 2$, which we refer to as the aperture source functions, are plotted in Fig. 2. In interpreting these plots one should bear in mind that the small and large spatial frequencies correspond to the far and near fields, respectively.

It follows from the Maxwell's equations that the aperture plane spectral fields may be propagated to any location z as [16]

$$\begin{bmatrix} \tilde{E}_x \\ \tilde{E}_y \end{bmatrix} = \begin{bmatrix} \tilde{E}_x^a \\ \tilde{E}_y^a \end{bmatrix} e^{-jk_z z}, \tag{14}$$

where

$$k_z = \sqrt{k^2 - k_\rho^2}, \quad \Im\mathrm{m}\, k_z \le 0\,. \tag{15}$$

The corresponding transverse magnetic field can then be determined as [19]

$$\begin{bmatrix} \tilde{H}_y \\ -\tilde{H}_x \end{bmatrix} = \frac{1}{k\eta k_z} \begin{bmatrix} k^2 - k_y^2 & k_x k_y \\ k_x k_y & k^2 - k_x^2 \end{bmatrix} \begin{bmatrix} \tilde{E}_x \\ \tilde{E}_y \end{bmatrix}, \tag{16}$$

and the axial field components as

$$\tilde{E}_z = -\frac{\eta}{k}\,(k_x \tilde{H}_y - k_y \tilde{H}_x), \tag{17}$$

$$\tilde{H}_z = -\frac{1}{k\eta}\,(k_y \tilde{E}_x - k_x \tilde{E}_y)\,. \tag{18}$$

What remains now is the Fourier inversion of the above expressions via (8). Switching to cylindrical coordinates, the two-dimensional Fourier-type integrals may be converted to one-dimensional Hankel transforms

$$\mathcal{S}_n\{\cdot\} \equiv \int_0^\infty \mathrm{d}k_\rho\, k_\rho\, J_n(k_\rho\rho)\, e^{-jk_z z}\,\{\cdot\}, \quad n = 0, 1, 2, \tag{19}$$

where J_n is the Bessel function of order n. As a result, we obtain the space domain fields as

$$\begin{aligned} E_x \;=\; & -\frac{2a^3}{3\pi}\,\kappa_{xi}\cos\psi_i\cos\varphi\,\mathcal{S}_1\{k_\rho F_1\} \\ & +\frac{2jka^3}{3\pi}\left[\cos\psi_i\left(\mathcal{S}_0\{(F_1+F_0)\} - \kappa_{xi}^2\mathcal{S}_0\{F_2\}\right)\right. \\ & \left.+\left(c_1+\kappa_{xi}^2\,\cos\psi_i\cos 2\varphi\right)\mathcal{S}_2\{F_2\}\right], \end{aligned} \tag{20}$$

$$\begin{aligned} E_y \;=\; & -\frac{2a^3}{3\pi}\,\kappa_{xi}\cos\psi_i\sin\varphi\,\mathcal{S}_1\{k_\rho F_1\} + \frac{2jka^3}{3\pi}\left[\kappa_{zi}\sin\psi_i\,\mathcal{S}_0\{(F_1+F_0)\}\right. \\ & \left.+\left(c_2+\kappa_{xi}^2\,\cos\psi_i\sin 2\varphi\right)\mathcal{S}_2\{F_2\}\right], \end{aligned} \tag{21}$$

$$\begin{aligned} E_z \;=\; & -\frac{2a^3}{3\pi}\,\kappa_{xi}\cos\psi_i\,\mathcal{S}_0\left\{\frac{k_\rho^2 F_1}{jk_z}\right\} \\ & -\frac{4jka^3}{3\pi}\left[c_3\,\mathcal{S}_1\left\{\frac{k_\rho F_0}{jk_z}\right\} - \kappa_{xi}^2\cos\psi_i\cos\varphi\,\mathcal{S}_1\left\{\frac{k_\rho F_2}{jk_z}\right\}\right], \end{aligned} \tag{22}$$

$$\begin{aligned} H_x \;=\; & \frac{2jka^3}{3\pi\eta}\,\kappa_{xi}\cos\psi_i\sin\varphi\,\mathcal{S}_1\left\{\frac{k_\rho F_1}{jk_z}\right\} \\ & +\frac{2k^2a^3}{3\pi\eta}\left[\kappa_{zi}\sin\psi_i\,\mathcal{S}_0\left\{\frac{F_1+F_0}{jk_z} - \frac{k_\rho^2}{k^2}\frac{F_1}{jk_z}\right\}\right. \\ & \left.+c_2\,\mathcal{S}_2\left\{\frac{F_2}{jk_z} - \frac{k_\rho^2}{k^2}\frac{F_1}{jk_z}\right\} + \kappa_{xi}^2\cos\psi_i\sin 2\varphi\,\mathcal{S}_2\left\{\frac{F_2}{jk_z}\right\}\right], \end{aligned} \tag{23}$$

$$\begin{aligned} H_y \;=\; & -\frac{2jka^3}{3\pi\eta}\,\kappa_{xi}\cos\psi_i\cos\varphi\,\mathcal{S}_1\left\{\frac{k_\rho F_1}{jk_z}\right\} \\ & -\frac{2k^2a^3}{3\pi\eta}\left[\cos\psi_i\left(\mathcal{S}_0\left\{\frac{F_1+F_0}{jk_z} - \frac{k_\rho^2}{k^2}\frac{F_1}{jk_z}\right\} - \kappa_{xi}^2\,\mathcal{S}_0\left\{\frac{F_2}{jk_z}\right\}\right)\right. \\ & \left.+c_1\,\mathcal{S}_2\left\{\frac{F_2}{jk_z} - \frac{k_\rho^2}{k^2}\frac{F_1}{jk_z}\right\} + \kappa_{xi}^2\cos\psi_i\cos 2\varphi\,\mathcal{S}_2\left\{\frac{F_2}{jk_z}\right\}\right], \end{aligned} \tag{24}$$

$$H_z = -\frac{4a^3}{3\pi\eta}\, c_4\, \mathcal{S}_1\{k_\rho F_1\}, \tag{25}$$

where we have introduced the notation

$$c_1 = \cos\psi_i \cos 2\varphi + \kappa_{zi} \sin\psi_i \sin 2\varphi, \tag{26}$$

$$c_2 = \cos\psi_i \sin 2\varphi - \kappa_{zi} \sin\psi_i \cos 2\varphi, \tag{27}$$

$$c_3 = \cos\psi_i \cos\varphi + \kappa_{zi} \sin\psi_i \sin\varphi, \tag{28}$$

$$c_4 = \cos\psi_i \sin\varphi - \kappa_{zi} \sin\psi_i \cos\varphi\,. \tag{29}$$

It should be noted that several terms in the above expressions drop out for a normally incident x-polarized plane wave, where $\kappa_{xi} = 0$ and $\sin\psi_i = 0$.

The field expressions (20)–(25) comprise Hankel transform integrals, which must be computed numerically. Since the integrations have to be redone for every distinct required value of ρ or z, the computational effort may be high, even if extrapolation is employed [20]. As an alternative, here we apply a complex image method, which leads to closed-form expressions for the electromagnetic fields, valid for all observation points.

3. COMPLEX IMAGE APPROXIMATION

Our complex image approach is based on the premise that each of the three aperture source functions can accurately be represented by a small number of complex exponential terms. To effect these approximations, we employ the so-called discrete complex image method (DCIM), which has been used to approximate Green functions

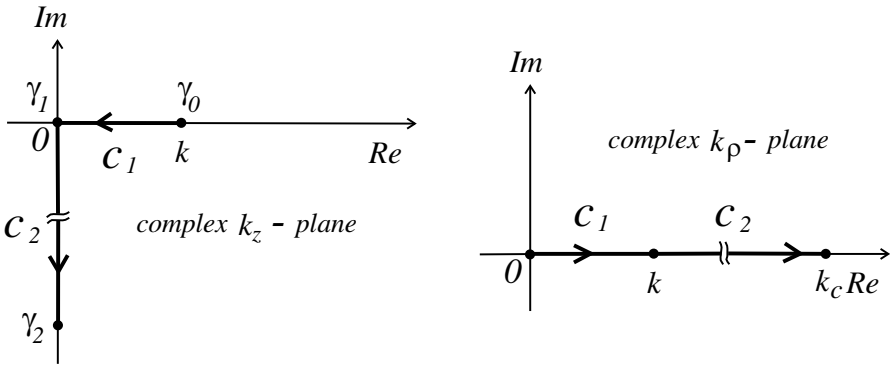

Figure 3. Linear sampling path segments in the k_z-plane and their mapping into the k_ρ-plane.

in layered media [21–23]. In the present case, we only need to perform three exponential fits

$$F_i(k_\rho a) \approx \sum_{n=1}^{N_i} \alpha_{in}\, e^{\beta_{in} t} = \sum_{n=1}^{N_i} a_{in}\, e^{-jk_z b_{in}},\ i = 0, 1, 2, \tag{30}$$

where t is a real sampling parameter and k_z is defined in (15). The exponential terms in the above expansions may be interpreted as arising from point sources, or images, located at complex-valued z coordinates b_{in}, hence the name of the method. To find the coefficients a_{in} and b_{in}, we employ the matrix pencil method (MPM) [24], which is based on a uniform sampling of (30) along one or more linear path segments in the complex k_z-plane, defined as

$$k_z = \gamma_{l-1} + (\gamma_l - \gamma_{l-1})\, t, \quad 0 \le t < 1, \tag{31}$$

where γ_ℓ are suitably selected nodes. The MPM returns the coefficients α_{in} and β_{in}, from which we find

$$b_{in} = \frac{j\beta_{in}}{\gamma_\ell - \gamma_{\ell-1}}, \quad a_{in} = \alpha_{in}\, e^{j\gamma_{\ell-1} b_{in}}. \tag{32}$$

We have adapted here the two-level approach of Aksun [21], with the sampling path segments C_l, $l = 1, 2$, as illustrated in Fig. 3. The k_z-plane nodes are at $\gamma_0 = k$, $\gamma_1 = 0$, and γ_2, where the latter is a user-specified point on the negative imaginary axis. These nodes map via (15) into the origin, k, and k_c of the k_ρ-plane, respectively. Note that the segments C_1 and C_2 contribute to the propagating and evanescent fields, respectively. In the two-level DCIM, we first sample on C_2, subtract the so-obtained exponential fit from the source function, and then sample the remainder again over C_1. This way, both the visible ($k_\rho < k$) and invisible ($k_\rho > k$) light ranges can accurately be captured. The sampling densities on these two segments and the desired accuracy of the fit must also be selected by the user. Hence, this approach requires a few trial-and-error computer runs to arrive at the suitable values for γ_2 (or k_c) and the sampling rates on C_2 and C_1. This process involves some trade-offs between efficiency and accuracy, where the latter can only be ascertained by comparisons with the results of a rigorous method, such as the spectral domain method using numerical quadrature. For our problem, we have found that excellent accuracy is obtained by choosing $k_c = 150/a$ and using 150 and 50 sampling points on C_2 and C_1, respectively. After this initial tuning, the DCIM is fully automatic, since the MPM determines the number of images N_i in (30) required for accurate exponential fits of the aperture source functions. With the parameters mentioned above, the resulting total number of images for each of the three functions F_i is around 20.

When the expansions (30) are substituted into (20)–(25), the Hankel transforms can be evaluated in closed forms with the help of Sommerfeld-type identities listed in Appendix A, which remain valid for complex-valued z coordinates [22]. As a result, we obtain

$$\begin{aligned}
\chi^e E_x &= -j\kappa_{xi} k\rho \cos\psi_i \cos\varphi \sum_{n=1}^{N_1} a_{1n} k z_{1n} B_{1n} \\
&\quad + \cos\psi_i \left(\sum_{i=0}^{1} \sum_{n=1}^{N_i} a_{in} k z_{in} A_{in} - \kappa_{xi}^2 \sum_{n=1}^{N_2} a_{2n} k z_{2n} A_{2n} \right) \\
&\quad + \left(c_1 + \kappa_{xi}^2 \cos\psi_i \cos 2\varphi\right) \sum_{n=1}^{N_2} a_{2n} \left(2D_{2n} - k z_{2n} A_{2n}\right), \qquad (33) \\
\chi^e E_y &= -j\kappa_{xi} k\rho \cos\psi_i \sin\varphi \sum_{n=1}^{N_1} a_{1n} k z_{1n} B_{1n} \\
&\quad + \kappa_{zi} \sin\psi_i \sum_{i=0}^{1} \sum_{n=1}^{N_i} a_{in} k z_{in} A_{in} \\
&\quad + \left(c_2 + \kappa_{xi}^2 \cos\psi_i \sin 2\varphi\right) \sum_{n=1}^{N_2} a_{2n} \left(2D_{2n} - k z_{2n} A_{2n}\right), \qquad (34) \\
\chi^e E_z &= j\kappa_{xi} \cos\psi_i \sum_{n=1}^{N_1} a_{1n} \left[2A_{1n} + (k\rho)^2 B_{1n}\right] \\
&\quad + 2k\rho \left[\kappa_{xi}^2 \cos\psi_i \cos\varphi \sum_{n=1}^{N_2} a_{2n} A_{2n} - c_3 \sum_{n=1}^{N_0} a_{0n} A_{0n} \right], \qquad (35) \\
\chi^h H_x &= j\kappa_{xi} k\rho \cos\psi_i \sin\varphi \sum_{n=1}^{N_1} a_{1n} A_{1n} + c_2 (k\rho)^2 \sum_{n=1}^{N_1} a_{1n} B_{1n} \\
&\quad + \kappa_{zi} \sin\psi_i \left\{ \sum_{i=0}^{1} \sum_{n=1}^{N_i} a_{in} G_{in} - \sum_{n=1}^{N_1} a_{1n} \left[2A_{1n} + (k\rho)^2 B_{1n}\right] \right\} \\
&\quad + \left(c_2 + \kappa_{xi}^2 \cos\psi_i \sin 2\varphi\right) \sum_{n=1}^{N_2} a_{2n} \left(2C_{2n} - G_{2n}\right), \qquad (36)
\end{aligned}$$

$$\begin{aligned}
\chi^h H_y \;=\; & -j\kappa_{xi} k\rho \cos\psi_i \cos\varphi \sum_{n=1}^{N_1} a_{1n} A_{1n} - c_1 (k\rho)^2 \sum_{n=1}^{N_1} a_{1n} B_{1n} \\
& - \cos\psi_i \left\{ \sum_{i=0}^{1} \sum_{n=1}^{N_i} a_{in} G_{in} - \sum_{n=1}^{N_1} a_{1n} \left[2A_{1n} + (k\rho)^2 B_{1n} \right] \right\} \\
& -2 \left(c_1 + \kappa_{xi}^2 \cos\psi_i \cos 2\varphi \right) \sum_{n=1}^{N_2} a_{2n} C_{2n} \\
& + \left[c_1 + \kappa_{xi}^2 \cos\psi_i (1 + \cos 2\varphi) \right] \sum_{n=1}^{N_2} a_{2n} G_{2n}, \qquad (37)
\end{aligned}$$

$$\chi^h H_z \;=\; 2c_4 k\rho \sum_{n=1}^{N_1} a_{1n} k z_{1n} B_{1n}, \qquad (38)$$

where we have introduced the notation

$$\chi^e \;=\; \frac{3\pi}{2j(ka)^3}, \quad \chi^h = \frac{3\pi\eta}{2(ka)^3}, \qquad (39)$$

$$G_{in} \;=\; \frac{e^{-jkr_{in}}}{kr_{in}}, \qquad (40)$$

$$A_{in} \;=\; (1 + jkr_{in}) \frac{G_{in}}{(kr_{in})^2}, \qquad (41)$$

$$B_{in} \;=\; \left[1 - 3 \frac{1 + jkr_{in}}{(kr_{in})^2} \right] \frac{G_{in}}{(kr_{in})^2}, \qquad (42)$$

$$C_{in} \;=\; \frac{1}{j(k\rho)^2} \left(e^{-jkz_{in}} - e^{-jkr_{in}} \right) \xrightarrow[\rho\to 0]{} \frac{e^{-jkz_{in}}}{2kz_{in}}, \qquad (43)$$

$$D_{in} \;=\; \frac{1}{(k\rho)^2} \left(e^{-jkz_{in}} - kz_{in} G_{in} \right) \xrightarrow[\rho\to 0]{} (1 + jkz_{in}) \frac{e^{-jkz_{in}}}{2(kz_{in})^2}, \qquad (44)$$

$$z_{in} \;=\; z + b_{in}, \quad r_{in} = \sqrt{\rho^2 + z_{in}^2}. \qquad (45)$$

Note that, since b_{in} are in general complex-valued, so are z_{in} and r_{in}. Note also that (43) and (44) have finite limits on the aperture axis.

We emphasize that the exponential fits (30) need only be performed once for a given electrical aperture radius ka. The resulting closed-form field expressions can then be used for any observation point in the $z > 0$ half-space. It should also be noted that some of the terms in the above field expressions appear more than once, and may thus be saved and reused to further improve the efficiency of computer simulations. Also, as already mentioned, several terms drop out for the normal incidence case.

4. SAMPLE NUMERICAL RESULTS

To illustrate the performance of the proposed complex image approach, we present sample computed results for both the normal and oblique incidence cases. The first set of results is for an aperture with $a = 10\,\text{nm}$, illuminated by a normally incident plane wave ($\kappa_{xi} = 0$, $\psi_i = 0°$) with $\lambda = 500\,\text{nm}$, so that $a/\lambda = 0.02$. In Fig. 4, we plot the electric and magnetic field components along the x axis for three different z values close to the aperture, and in Fig. 5 similar plots are presented along the y axis. Not shown in these figures are plots of E_y and H_x, which identically vanish along the x and y axes. Note the expected near-singularity of the field components normal to the aperture edge. As a check for our complex image method, we also include in the above figures the corresponding results obtained by the rigorous spectral domain approach.

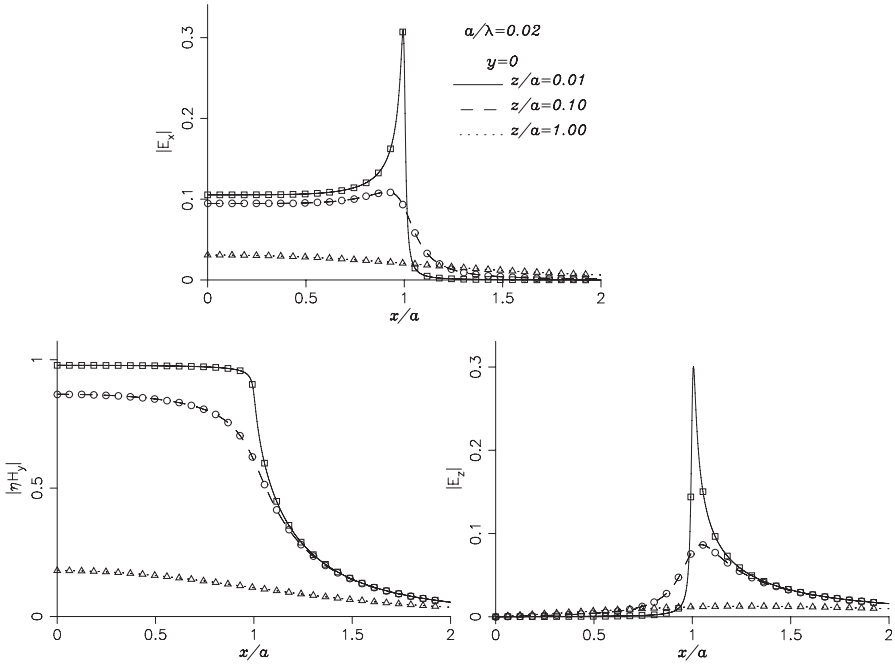

Figure 4. Electric and magnetic field plots along the x axis for $a/\lambda = 0.02$ and $z/a = 0.01$, 0.1, and 1.0. The symbols indicate the corresponding results obtained by the rigorous spectral domain method.

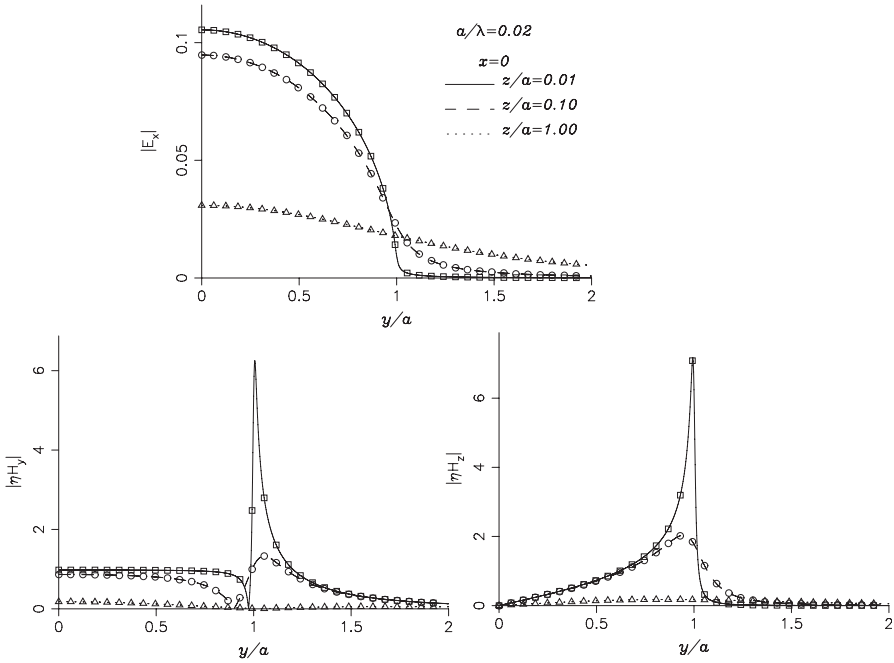

Figure 5. As in Fig. 4, except that the plots are along the y axis.

For the same aperture and incidence, in Figs. 6(a) and (b) we present surface plots of the magnitude of the time-average Poynting vector in two planes parallel to the screen at $z = a/10$ and $z = a$, respectively. In the first case, we note the expected appearance of two "hot spots" where the x-polarized electric field of the incident wave is perpendicular to the aperture edges. In the second case, only a single peak is observed, centered at the aperture axis. We have obtained virtually the same plots by the rigorous spectral domain approach using adaptive quadrature and extrapolation [20], with the maximum discrepancy between the two methods not exceeding 0.1%. However, the complex image approach was more than 50 times faster than the already accelerated rigorous method.

The second set of results is for an aperture of radius $a = 50\,\text{nm}$, illuminated by an obliquely incident plane wave at $\lambda = 600\,\text{nm}$, so that $a/\lambda \approx 0.083$. This is an example of a larger aperture, previously analyzed for normal incidence by Stevenson and Richards [16]. For the oblique incidence case, no reliable published data are available for comparison. We begin with field plots along the aperture axis for z extending from a small fraction of a into the radiation zone,

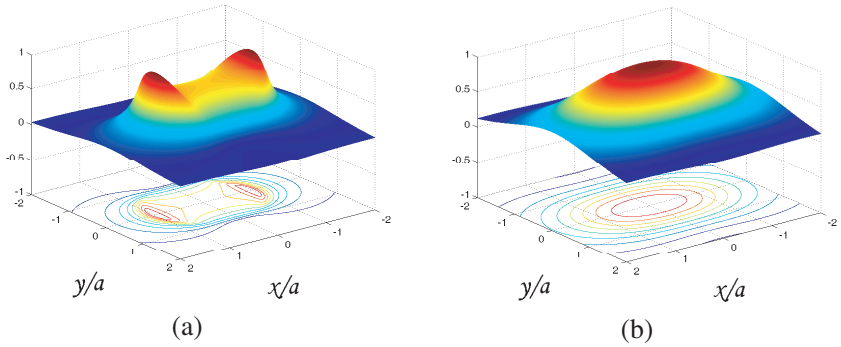

Figure 6. Plots of the magnitude of the time-average Poynting vector in two planes parallel to the screen for $a/\lambda = 0.02$. The plots in (a) and (b) are for $z = a/10$ and $z = a$, respectively, and are normalized to the maximum values, which are $4.195 \times 10^{-5}/\eta$ and $1.176 \times 10^{-5}/\eta$, respectively.

under TM ($\psi_i = 0°$) and TE ($\psi_i = 90°$) excitation. The results in Figs. 7 and 8 are for a homogeneous plane wave ($\kappa_{xi} = 0.5, \theta_i = 30°$) and the results in in Figs. 9 and 10 are for an evanescent plane wave ($\kappa_{xi} = 3$). The field components not shown are identically zero on the z axis. For comparison we also include in these figures the results obtained by the quasi-static theory [6], valid in the near zone, and by the equivalent dipole method [25], applicable in the far zone. We note that the complex image method results (solid lines) follow the quasi-static results (dotted lines) in the near zone and then transition to the equivalent dipole results (dashed lines) farther from the aperture. Also, as already noted by Leviatan [9], the transmitted field magnitude remains approximately constant up to $z \approx a$, and then decreases precipitously, reaching the drop off rate of $1/z$ for $z > 10a$. The magnetic field plots exhibit a distinct intermediate zone with a drop off rate of $1/z^2$. Comparing the homogeneous and evanescent illumination results, we note a significant near-zone electric field enhancement in the latter case, with a concomitant enhancement in transmission efficiency [17]. For the evanescent TM wave, we note a null in the axial plot of $|E_x|$, which is a near-field phenomenon also predicted by the quasi-static analysis. We have observed that this null appears near the aperture as soon as $\kappa_{xi} > \sqrt{2}$ and moves away with increasing κ_{xi}.

For the same aperture ($a/\lambda = 0.083$) and TM plane wave ($\psi_i = 0°$), in Fig. 11 we present plots of the time-average Poynting vector

in the xz-plane in the range $-2a < x < 2a$ and $0.1a < z < a$. The three plots shown are for $\kappa_{xi} = 0$ (normal incidence), $\kappa_{xi} = 0.5$ ($\theta_i = 30°$), and $\kappa_{xi} = 3$ (evanescent wave incidence). The vectors at any fixed longitudinal distance z from the aperture are normalized

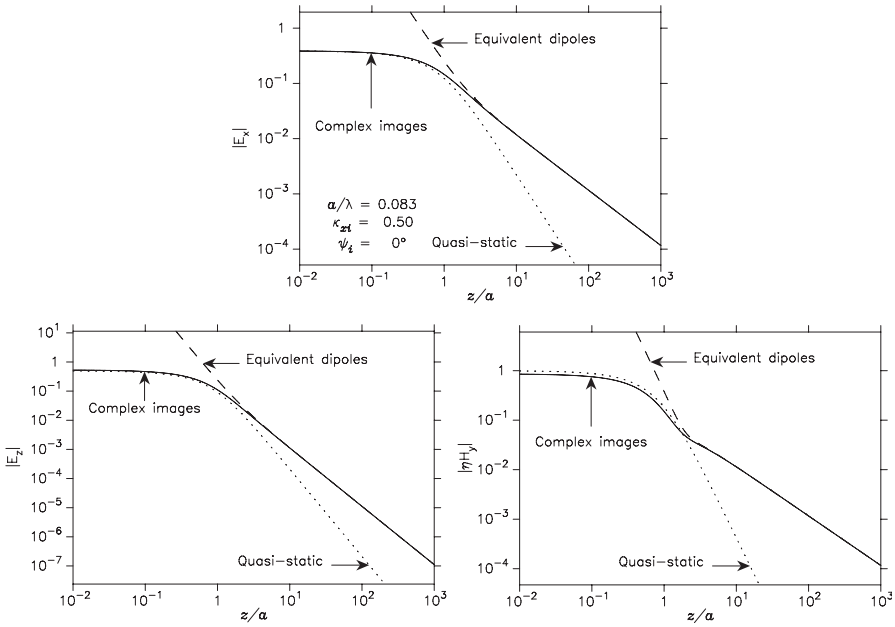

Figure 7. Axial plots of the electric and magnetic field components for $a/\lambda = 0.083$, $\psi_i = 0°$, and $\kappa_{xi} = 0.5$ ($\theta_i = 30°$) (homogeneous TM wave incidence).

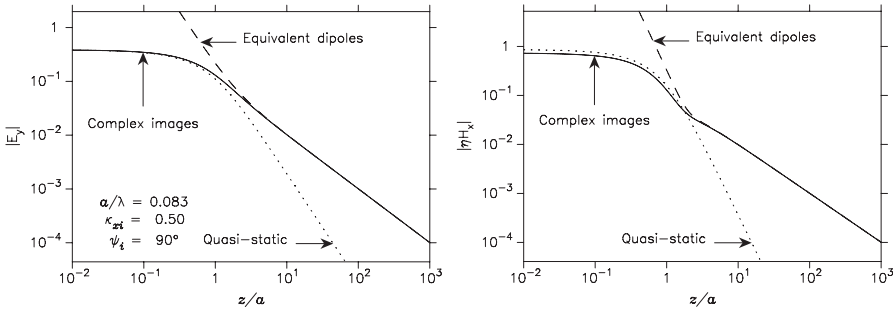

Figure 8. As in Fig. 7, except that $\psi_i = 90°$ (homogeneous TE wave incidence).

to the maximum magnitude at the same z coordinate, in order to clearly show the direction of the power flux in the entire z range considered. The magnitude distribution information is provided by the constant level contours superposed on the vector plots, with the level separation of one-tenth of the maximum value, where the latter

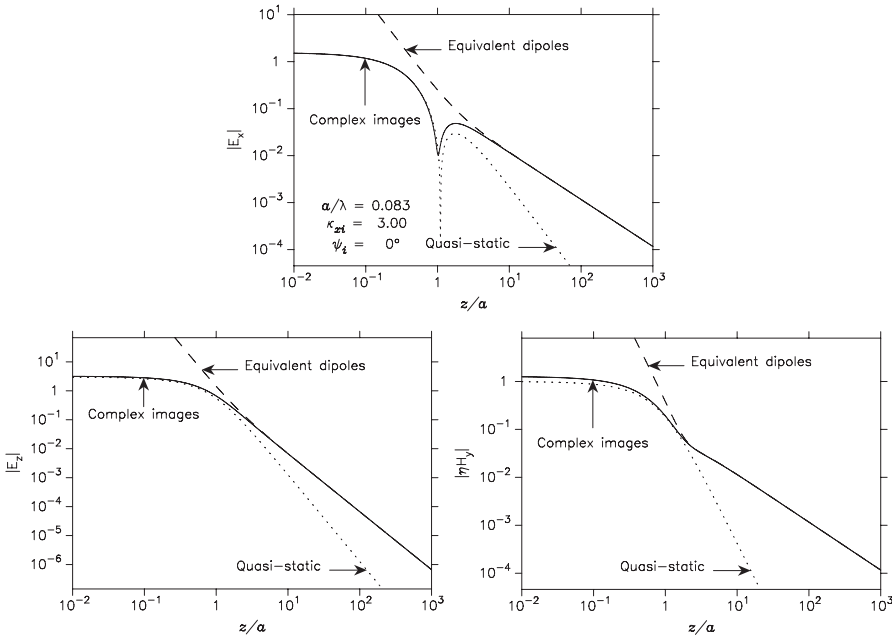

Figure 9. Axial plots of the electric and magnetic field components for $a/\lambda = 0.083$, $\psi_i = 0°$, and $\kappa_{xi} = 3$ (evanescent TM wave incidence).

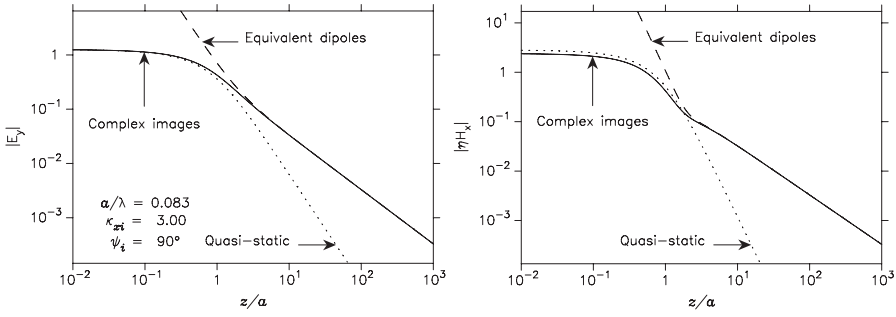

Figure 10. As in Fig. 9, except that $\psi_i = 90°$ (evanescent TE wave incidence).

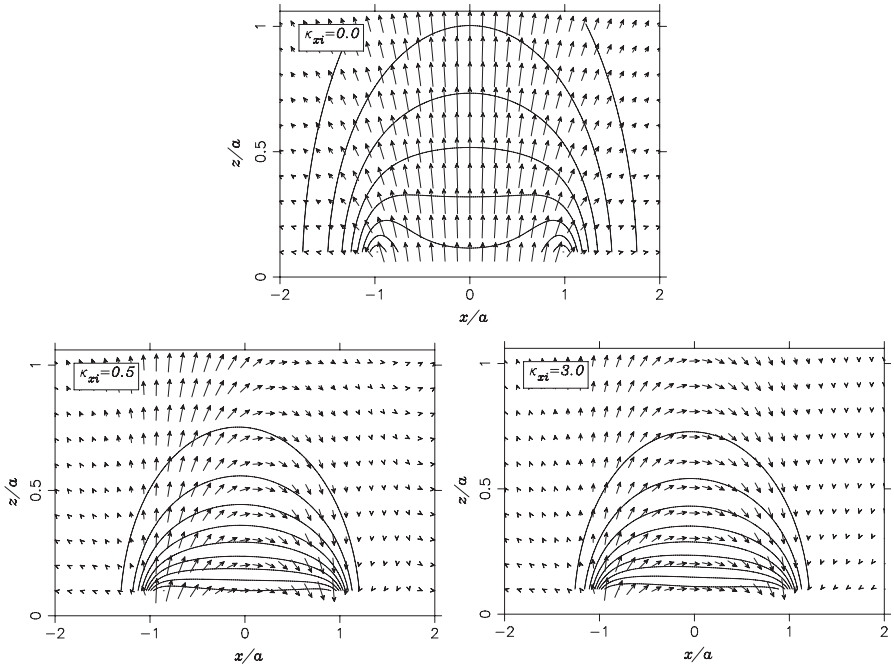

Figure 11. Plots of the time-average Poynting vector in the xz-plane for an aperture with $a/\lambda = 0.083$, excited by a TM plane wave ($\psi_i = 0°$) with different angles of incidence.

corresponds to the contour closest to the aperture. We note that for the normal incidence case the power flux is directed away from the aperture, as expected. Under oblique incidence, however, the power tends to flow along semi-circular paths returning to the aperture and the power-flux density is stronger and more confined to the aperture region. For the homogeneous wave case this was previously observed by Nakano and Kawata [11]. These effects are further enhanced for the evanescent wave illumination, where the Poynting vector plot is nearly symmetric and the power flow is nearly transverse along the aperture axis. The dip in the axial plot of $|E_x|$ observed in Fig. 9 is clearly responsible for the vanishing of the axial component of the Poynting vector on the z axis at some distance from the aperture in the plot corresponding to $\kappa_{xi} = 3$.

5. CONCLUSION

We have presented an efficient complex image method for the analysis of a subwavelength circular aperture in a perfectly conducting screen of infinitesimal thickness, illuminated by a plane wave, which may be obliquely incident and evanescent. The method is based on the Bethe-Bouwkamp (BB) quasi-static model of the aperture and the spectral domain formulation of the problem. In the spectral domain approach, the fields are expressed as Hankel transforms, which must be evaluated numerically for every distinct observation point of interest. The key step in the proposed method is the approximation of three so-called aperture source functions, which characterize the spectrum of the BB aperture field, in terms of a small number of complex exponential terms. This makes it possible to evaluate the Hankel transforms analytically, resulting in closed-form expressions for the electric and magnetic field components, valid for all observation points.

The complex image method results are in excellent agreement with those of a rigorous spectral domain method using numerical quadrature with extrapolation. However, in a typical case the complex image method is more than 50 times faster than the already accelerated rigorous method. Hence, the spectral domain complex image method presented here is a useful alternative to other available techniques for the modeling of the aperture sources in scanning near-field optical microscopy.

We have included sample results showing a circulating power flux and enhanced field confinement under oblique incidence. These effects are further amplified when the aperture is illuminated by an inhomogeneous (evanescent) plane wave.

APPENDIX A. HANKEL TRANSFORM IDENTITIES

The identities used in the closed-form Hankel transform inversion are

$$\int_0^\infty dk_\rho k_\rho J_0(k_\rho\rho)\frac{e^{-jk_z z}}{jk_z} = G, \tag{A1}$$

$$\int_0^\infty dk_\rho k_\rho J_0(k_\rho\rho)e^{-jk_z z} = z(1+jkr)\frac{G}{r^2}, \tag{A2}$$

$$\int_0^\infty dk_\rho k_\rho^3 J_0(k_\rho\rho)\frac{e^{-jk_z z}}{jk_z} = 2(1+jkr)\frac{G}{r^2}+(k\rho)^2\left[1-3\frac{1+jkr}{(kr)^2}\right]\frac{G}{r^2}, \tag{A3}$$

$$\int_0^\infty dk_\rho k_\rho^2 J_1(k_\rho\rho)\frac{e^{-jk_z z}}{jk_z} = \rho(1+jkr)\frac{G}{r^2}, \tag{A4}$$

$$\int_0^\infty dk_\rho k_\rho^2 J_1(k_\rho\rho)e^{-jk_z z} = -k^2\rho z\left[1-3\frac{1+jkr}{(kr)^2}\right]\frac{G}{r^2}, \tag{A5}$$

$$\int_0^\infty dk_\rho k_\rho J_2(k_\rho\rho)\frac{e^{-jk_z z}}{jk_z} = \frac{2}{jk\rho^2}\left(e^{-jkz}-rG\right)-G, \tag{A6}$$

$$\int_0^\infty dk_\rho k_\rho J_2(k_\rho\rho)e^{-jk_z z} = \frac{2}{\rho^2}\left(e^{-jkz}-zG\right)-z(1+jkr)\frac{G}{r^2}, \tag{A7}$$

$$\int_0^\infty dk_\rho k_\rho^3 J_2(k_\rho\rho)\frac{e^{-jk_z z}}{jk_z} = -(k\rho)^2\left[1-3\,\frac{1+jkr}{(kr)^2}\right]\frac{G}{r^2}, \tag{A8}$$

where

$$G=\frac{e^{-jkr}}{r}, \quad r=\sqrt{\rho^2+z^2}, \tag{A9}$$

and k_z is given by (15). Note that the first identity above is the well-known Sommerfeld identity [26, p. 66], from which the other identities can be derived.

REFERENCES

1. Thio, T., K. M. Pellerin, R. A. Linke, and H. J. Lezec, "Enhanced light transmission through a single subwavelength aperture," *Opt. Lett.*, Vol. 26, 1972–1974, 2001.
2. Ducourtieux, S., S. Grésillon, J. C. Rivoal, C. Vannier, C. Bainier, D. Courjon, and H. Cory, "Imaging subwavelength holes in chromium films in scanning near-field optical microscopy. Comparison between experiments and calculation," *Eur. Phys. J. Appl. Phys.*, Vol. 26, 35–43, 2004.
3. Lin, Y., M. H. Hong, W. J. Wang, Z. B. Wang, G. X. Chen, Q. Xie, L. S. Tan, and T. C. Chong, "Surface nanostructuring by femtosecond laser irradiation through near-field scanning optical microscopy," *Sens. Actuators A*, Vol. 133, 311–316, 2007.
4. Bethe, H. A., "Theory of diffraction by small holes," *Phys. Rev.*, Vol. 66, 163–182, Oct. 1944.
5. Bouwkamp, C. J., "On Bethe's theory of diffraction by small holes," *Philips Res. Rep.*, Vol. 5, 321–332, Oct. 1950.
6. Bouwkamp, C. J., "Diffraction theory. A critique of some recent developments," Math. Res. Group, Res. Rep. No. EM-50, New York University, Washington Sq. College of Arts and Science, New York, Apr. 1953.

7. Bouwkamp, C. J., "Diffraction theory," *Rep. Progr. Phys.*, Vol. 17, 35–100, 1954.
8. Dunn, R. C., "Near-field scanning optical microscopy," *Chem. Rev.*, Vol. 99, 2891–2927, 1999.
9. Leviatan, Y., "Study of near-zone fields of a small aperture," *J. Appl. Phys.*, Vol. 60, No. 5, 1577–1583, 1986.
10. Dürig, U., D. W. Pohl, and F. Rohner, "Near-field optical-scanning microscopy," *J. Appl. Phys.*, Vol. 59, No. 10, 3318–3327, 1986.
11. Nakano, T. and S. Kawata, "Numerical analysis of the near-field diffraction pattern of a small aperture," *J. Mod. Opt.*, Vol. 39, No. 3, 645–661, 1992.
12. Van Labeke, D., D. Barchiesi, and F. Baida, "Optical characterization of nanosources used in scanning near-field optical microscropy," *J. Opt. Soc. Am. A*, Vol. 12, No. 4, 695–703, 1995.
13. Van Labeke, D., F. I. Baida, and J. Vigoureux, "A theoretical study of near-field detection and excitation of surface plasmons," *Ultramicroscopy*, Vol. 71, 351–359, 1998.
14. Baida, F. I. and D. Van Labeke, "Propagation and diffraction of locally excited surface plasmons," *J. Opt. Soc. Am. A*, Vol. 18, 1552–1561, July 2001.
15. Grober, R. D., T. Rutherford, and T. D. Harris, "Modal approximation for the electromagnetic field of a near-field optical probe," *Appl. Opt.*, Vol. 35, 3488–3494, July 1996.
16. Stevenson, R. and D. Richards, "The use of a near-field probe for the study of semiconductor heterostructures," *Semicond. Sci. Technol.*, Vol. 13, 882–886, 1998.
17. Petersson, L. E. R. and G. S. Smith, "Transmission of an inhomogeneous plane wave through an electrically small aperture in a perfectly conducting plane screen," *J. Opt. Soc. Am. A*, Vol. 21, No. 6, 975–980, 2004.
18. Harrington, R. F., *Time-Harmonic Electromagnetic Fields*, McGraw-Hill, New York, 1961.
19. Lin, C., K. M. Leung, and T. Tamir, "Modal transmission-line theory of three-dimensional periodic structures with arbitrary lattice configurations," *J. Opt. Soc. Am. A*, Vol. 19, 2005–2017, Oct. 2002.
20. Michalski, K. A., "Extrapolation methods for Sommerfeld integral tails (Invited review paper)," *IEEE Trans. Antennas Propagat.*, Vol. 46, 1405–1418, Oct. 1998.
21. Aksun, M. I., "A robust approach for the derivation of closed-

form Green's functions," *IEEE Trans. Microwave Theory Tech.*, Vol. 44, 651–658, May 1996.

22. Li, Y. L. and M. J. White, "Near-field computation for sound propagation above ground — Using complex image theory," *J. Acoust. Soc. Am.*, Vol. 99, 755–760, Feb. 1996.
23. Alparslan, A., M. I. Aksun, and K. A. Michalski, "Closed-form Green's functions in planar layered media for all ranges and materials," *IEEE Trans. Microwave Theory Tech.*, Vol. 58, 602–613, Mar. 2010.
24. Sarkar, T. K. and O. Pereira, "Using the matrix pencil method to estimate the parameters of a sum of complex exponentials," *IEEE Antennas Propagat. Magaz.*, Vol. 37, 48–55, Feb. 1995.
25. Rahmat-Samii, Y. and R. Mittra, "Electromagnetic coupling through small apertures in a conducting screen," *IEEE Trans. Antennas Propagat.*, Vol. 25, 180–187, Mar. 1977.
26. Chew, W. C., *Waves and Fields in Inhomogeneous Media*, IEEE Press, New York, 1995.